**Supporting information**

***for***

# Sacrificial $MoO_4^{2-}$ Containing Ni/Co-(Pre)catalysts: Understanding of Active Structure and Fe-Dynamics under Steady-state Conditions in Alkaline Oxygen Electrocatalysis

*Indranil Mondal*, Anisha Mondal, Anumod CA, Subhash Chandra Shit*

## 1. Experimental Section

### 1.1. Materials

Ammonium heptamolybdate ($(NH_4)_6Mo_7O_{24}.4H_2O$), cobalt nitrate ($Co(NO_3)_2.6H_2O$, 98%), and nickel nitrate ($Ni(NO_3)_2.6H_2O$, 97%) were purchased from Sigma Aldrich. Analytical-grade biological diluent (ethanol) was purchased from HiMedia. Sodium hydroxide and potassium hydroxide (85%) were purchased from Alfa Aesar. Fluorine-doped tin oxide (FTO) of surface resistivity 7 Ω was purchased from Sigma Aldrich. All the reagents were used without any further purification.

### 1.2. Material Synthesis

#### 1.2.1. Synthesis of cobalt molybdate ($CoMoO_4$)

In a glass vial, 1 mmol of $Co(NO_3)_2.6H_2O$ was dissolved in 10 ml of deionized (DI) water and aged for 30 min at 80 ˚C. In another vial, 2 mmol of $(NH_4)_6Mo_7O_{24}.4H_2O$ was dispersed in 10 ml of DI water, and the resulting solution was added dropwise into the $Co^{2+}$ solution with a mixing rate of 1 ml/min. After complete addition, at 80 ˚C, the solution was aged for 3-4 hours with the closed lid of the vial. Once the violet color precipitate formation was completed, it was washed with a 1:1 ethanol-water mixture and dried at 60˚C overnight.

## 2. Materials' Characterization

X-ray diffraction patterns for materials were obtained from PANalytical powder XRD. Here, a position-sensitive detector, a curved germanium (111) primary monochromator, and Cu-$K_{\alpha 1}$ radiation ($\lambda$ = 1.5418 Å) were used. Scanning Electron Microscopy (SEM) was done to analyze the morphologies using an FEI NOVA NANOSEM 450 field emission scanning electron microscope under 10 kV electron gun energy. For mapping and elemental analysis, the SEM measurements were performed using 15 kV electron gun energy integrated with an energy

dispersive X-ray (EDX) detector (Bruker Quantax XFlash® 6|60). Data handling and analyses were attained with the software package EDAX. The high-resolution TEM, HAADF-STEM, and the corresponding energy dispersive spectroscopy mapping analyses were performed on an FEI TECNAI G2 F30) transmission electron microscope (TEM 300kV) equipped with a $LaB_6$ source. The catalyst films were scratched off from the FTO substrate and transferred onto a carbon-coated copper grid for their investigation after catalysis. EDX analyses were achieved with an EDAX r-TEM SUTW (Si (Li) detector). GATAN MS794 P and GATAN US1000 CCD cameras were used to collect the images. The scanning TEM (STEM) experiments were conducted on a probe-corrected JEM-ARM300F2 "GrandARM2" (JEOL Ltd.) with a cold-FEG emitter at 80 and 300 kV, equipped with 2 x 158mm² windowless SDD-EDX detectors with a solid angle of 2.2 sr. HAADF images correspond to detection angles of 54-220 mrad. The X-ray photoelectron spectra (XPS) were acquired using an Omicron X-ray photoelectron spectrometer using Mg-$K_\alpha$ radiation at 1253.6 eV as the excitation source with an Al-$K_\alpha$ monochromatic radiation source (1486.7 eV) with a 90° take-off angle (normal to analyzer). The vacuum pressure in the analyzing chamber was set at $2 \times 10^{-9}$ Torr. The XPS spectra were collected for C 1s, O 1s, Ni 2p, Co 2p, and Mo 3d levels with a pass energy of 20 eV and a step of 0.1 eV. The binding energies were calibrated relative to the C 1s peak energy position as 285.0 eV. Data analyses were carried out using Casa XPS (Casa Software Ltd.) and the Vision data processing program (Kratos Analytical Ltd.). For ICP-AES analysis, the solid materials are digested in a minimum quantity of supelco 60% $HNO_3$ (Merck) and diluted with HPLC-grade water. The standard solutions were prepared using TraceCERT®, 1 mg/L Ni/Fe in nitric acid solution. The Ni and Fe were standardized at 221.3 nm and 238.6 nm, respectively.

### *In situ* Raman spectroscopy

The *in-situ* Raman spectra were recorded by exciting the samples using a 532 nm argon laser. A confocal Raman spectrometer associated with a liquid nitrogen-cooled charge-coupled device camera as a detector (Renishaw). Water-immersion objective lens (40XW, Olympus, numerical aperture: 0.8) covered with PFA film (0.05 mm thickness) was used in the home-built single chamber electrochemical cell. During measurement, a noncontact probe head with a working distance of 5 cm and a sample spot size of 1 mm was used. For every measurement, a 5s acquisition time was required. To record the Raman spectra, the electrochemically activated Ni/$CoMoO_4$/FTO film is used.

**Electrophoretic deposition and electrochemical measurements**

The investigated materials were electrophoretically deposited (EPD) on thoroughly cleaned fluorine-doped tin oxide (FTO) by applying a potential difference of 10 V in a mixture of iodine and acetone.[1] The deposition was carried out on a 1 × 1 $cm^2$ area. For a typical deposition, 40 mg of the catalyst powder was suspended in 10 mL of acetone, and 2 mg of iodine was then added. This solution is sonicated for 15 min and taken in a 10 ml glass beaker. Before EPD, the empty electrodes were weighed using an analytical balance. After each EPD, the increase in weight of the electrodes was monitored carefully.

The electrochemical testing was carried out in a standard three-electrode (working, counter, and reference) electrochemical cell in 1 M aqueous KOH with a potentiostat (VMP3,16 channel potentiostat from BioLogic Science Instruments) controlled by the EC-Lab v10.20 software package. The electrodes (FTO) with deposited catalysts served as the working electrodes, Pt wire (0.5 mm diameter from DTech solution) as a counter, and Hg/HgO (D-Tech solution) as the reference electrode. All potentials presented in this work were transferred to the RHE scale by calibrating the reference electrodes versus an RHE electrode (+917 mV for 1 M KOH (pH 13.89).[2]

The chronoamperometric measurements were performed in 1 M aqueous KOH at selected constant potentials with respect to RHE.

The voltammograms and chronoamperometry curves were recorded with an applied *iR* compensation of 90%. The uncompensated resistance was obtained from an impedance point measurement at 1.2 $V_{RHE}$ and 100 kHz with an amplitude of 10 mV. Tafel plots were calculated by potentiostatic measurements between 1.4 and 1.6 $V_{RHE}$, employing stepwise potential changes by 20 mV. The current density at each potential was determined by taking the average of a 2-minute measurement. The Tafel slope was calculated according to the Tafel equation $\eta = b\log j + a$, where $\eta$ is overpotential (V), $j$ is the current density (mA $cm^{-2}$), and $b$ is the Tafel slope ($mVdec^{-1}$) and a is the intercept of the plot which is proportional to exchange current density ($j^0$). The commercial KOH solution was made Fe-free using freshly made $Ni(OH)_2$. Briefly, the Fe-free 1 M KOH was prepared using readily prepared $Ni(OH)_2$ .[3] Briefly, 2 M KOH solution was dropwise added to a 10 ml solution of 5 mmol $Ni(NO_3)_2.6H_2O$ with constant stirring. The resulting green $Ni(OH)_2$ precipitate was centrifuged and washed with Milli-Q water. Subsequently, 30 ml of commercial 1 M KOH solution was added to the as-prepared

$Ni(OH)_2$ and stirred for 15 min, followed by keeping it overnight for resting. Finally, the mixture was centrifuged, and the solution was collected for electrochemical measurements.


**Scheme S1**. Stepwise synthesis mechanism for the MMoO4. $xH_2O$ (M = Co, Ni)

**Table S1**. Averaged lengths of *M*–O bonds in respective polyhedra.

| **Hydrates** | **Polyhedra** | **Averaged lengths (Å)** |
|---|---|---|
| $NiMoO_4 \cdot 3/4H_2O$<br>*a*, *b*, *c*/Å = 6.7791(2), 6.8900(2), 9.2486(2)<br>*α*, *β*, *γ* /° = 76.681(2), 83.960(2), 74.218(2) | $NiO_6$ | 2.06 |
| | $NiO_5(OH_2)$ | 2.03 |
| | $MoO_4 \equiv (1)$ | 1.79 |
| | $MoO_4 \equiv (2)$ | 1.78 |
| | | |
| $CoMoO_4 \cdot 3/4H_2O$<br>*a*, *b*, *c*/Å = 6.844(2), 6.933(2), 9.339(2)<br>*α*, *β*, *γ* /° = 76.617(3), 84.188(7) 74.510(8) | $CoO_6$ | 2.08 |
| | $CoO_5(OH_2)$ | 2.09 |
| | $MoO_4 \equiv (1)$ | 1.75 |
| | $MoO_4 \equiv (2)$ | 1.74 |

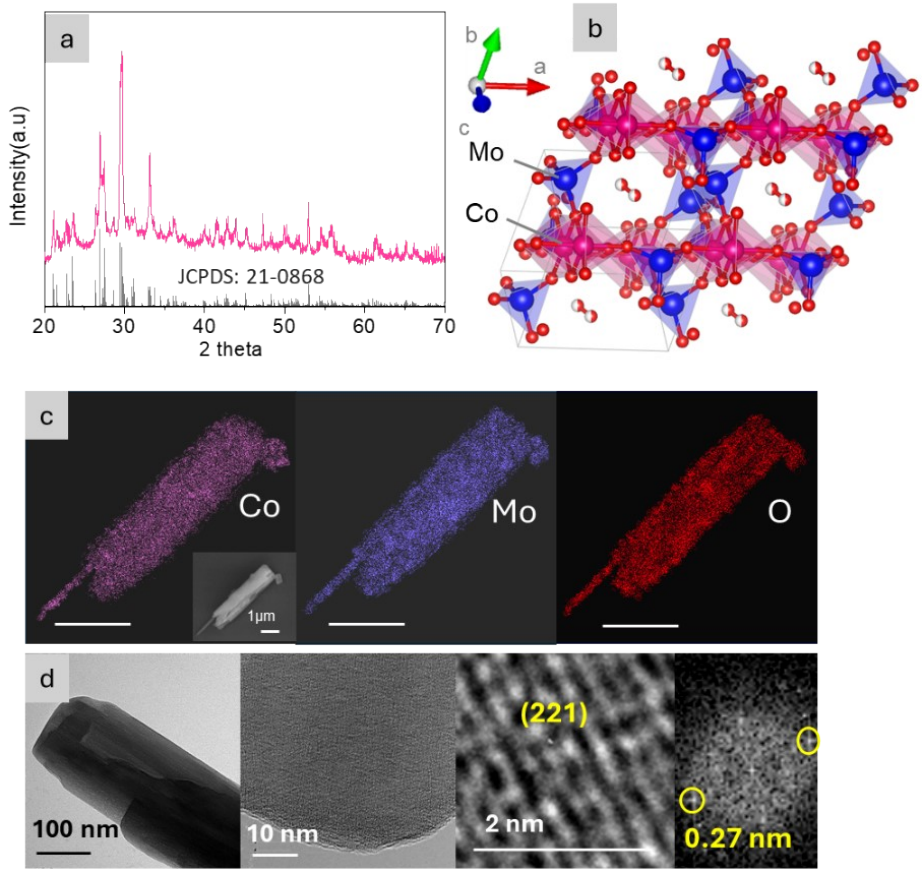


**Fig. S1** (a) The XRD pattern of the sample matches the reported JCPDS file and exhibits sharp reflections. (b) Crystal structure of $CoMoO_4 \cdot xH_2O$. The blue tetrahedra and purple octahedra imply the $[MoO_4]$ and $[CoO_6]$ units, respectively. (c) SEM and corresponding elemental mapping (in 1 μm scale) reveal the homogeneous distribution of the elements and smooth crystallite surface. (d) Low magnification and HR-TEM further support the smooth crystallite surface with no surface oxidation. FFT of the HR-TEM confirms the lattice distance of 0.27 nm that corresponds to the (221) plane.

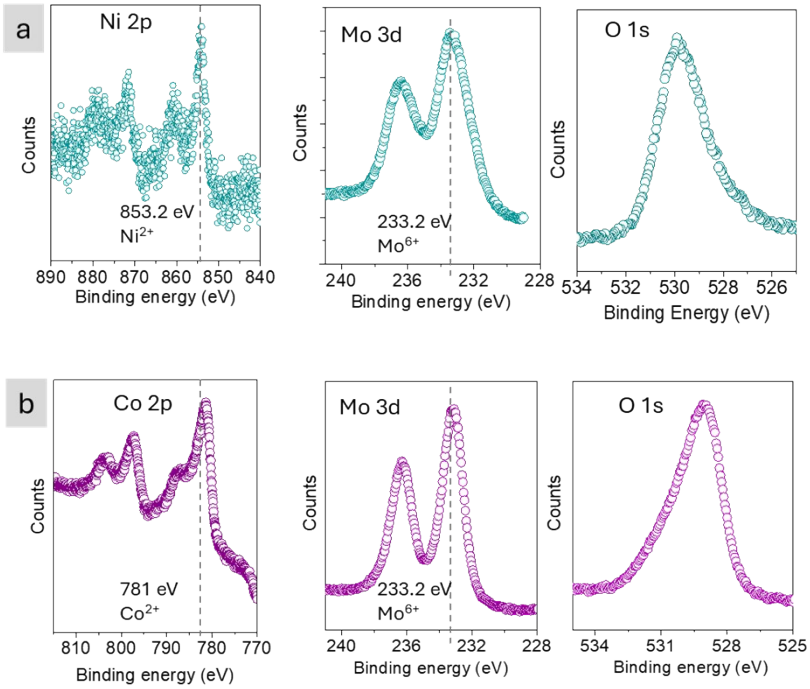


**Fig. S2** High resolution XPS profile of as-prepared (a) $NiMoO_4 \cdot xH_2O$ and (b) $CoMoO_4 \cdot xH_2O$.

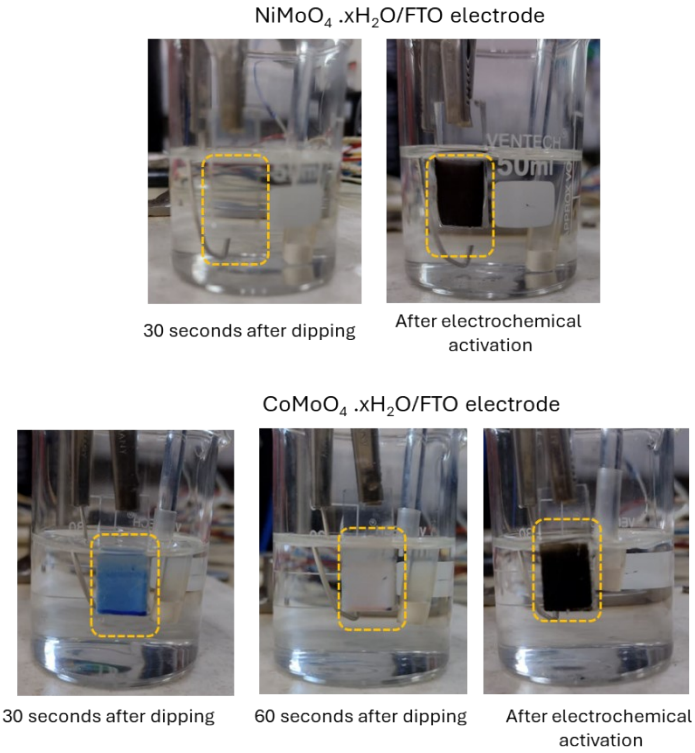


**Fig. S3** The color of the $MMoO_4.xH_2O$ deposited on FTO (M = Ni, Co) in 1 M KOH under different conditions.

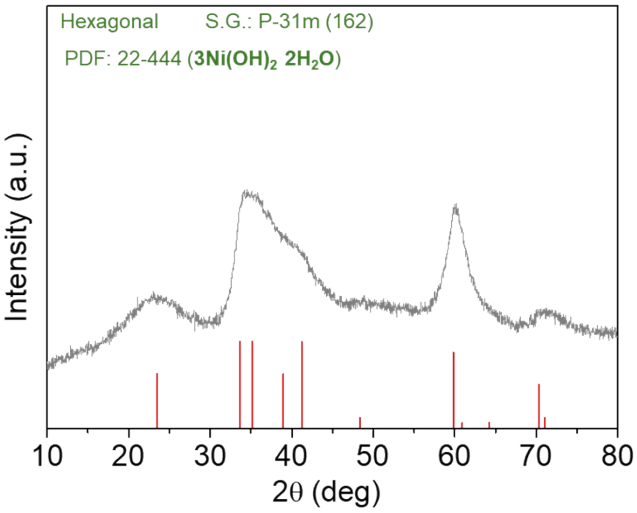


**Fig. S4** Powder XRD of $NiMoO_4 \cdot xH_2O$ aged in 1 M KOH. The result indicates the leaching of Mo species and the formation of a hydroxo phase of Ni.

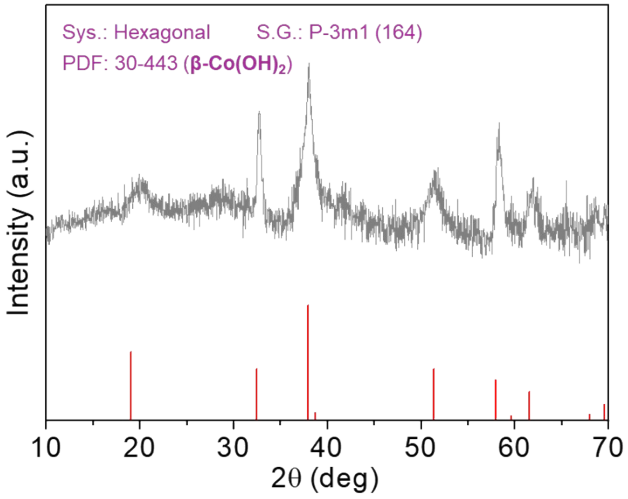


**Fig. S5** Powder XRD of $CoMoO_4 \cdot xH_2O$ aged in 1 M KOH. The result indicates the leaching of Mo species and the formation of a Co-hydroxo phase.

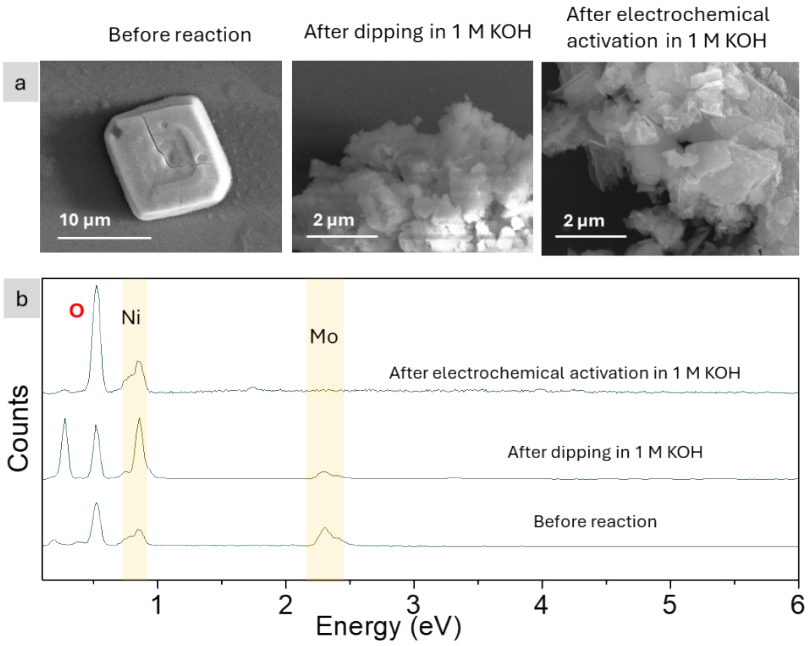


**Fig. S6** (a)SEM image and (b) SEM-EDX profile of the $NiMoO_4 \cdot xH_2O$. After dipping into the KOH, the sample lost more than 90% of the Mo species.

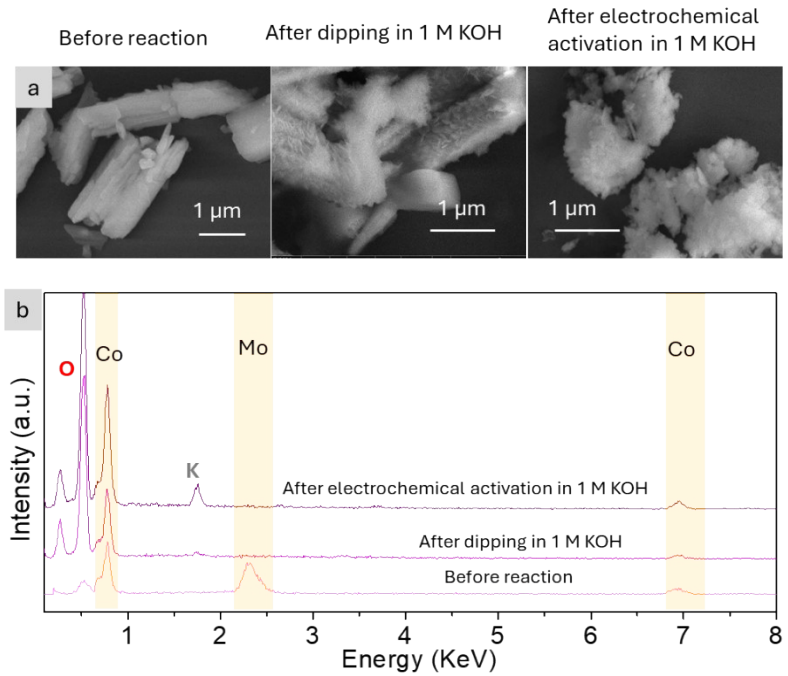


**Fig. S7** (a)SEM image and (b) SEM-EDX profile of the $CoMoO_4 \cdot xH_2O$. After dipping into the KOH, the sample lost the complete Mo species.

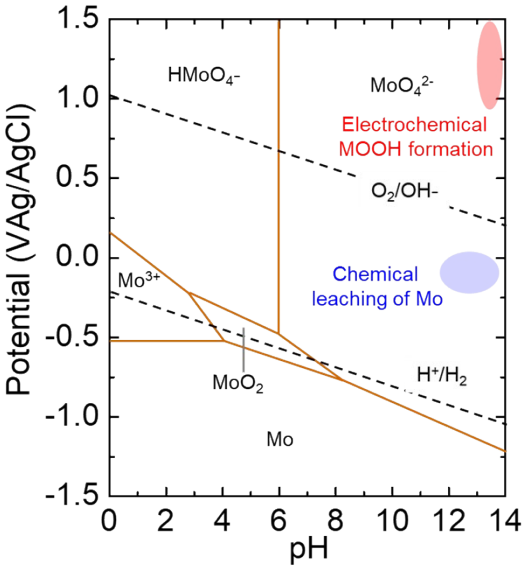


**Fig. S8** Pourbaix diagram of the Mo-$H_2O$ at 25˚C. Possible chemical and electrochemical dissolution of Mo-oxo species is depicted in the diagram. The diagram is conceptualized from.[4]

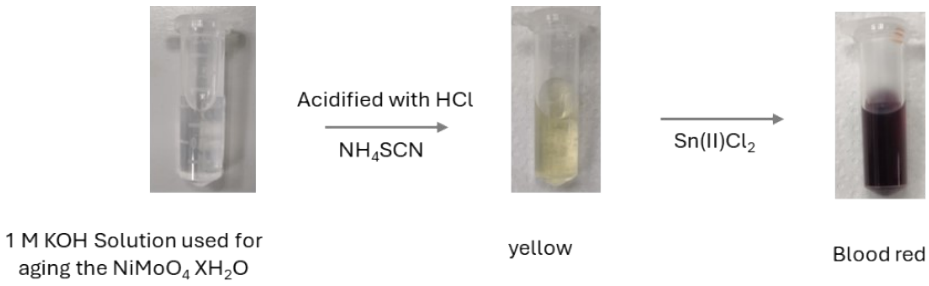


**Fig. S9** Thiocyanide-based confirmatory test with electrolyte solution used for aging the $NiMoO_4 \cdot xH_2O$ (taken as a representative example). Since this experiment requires more than 100 mg of sample, it cannot be performed with FTO-deposited samples, as they contain less than 1 mg of sample.

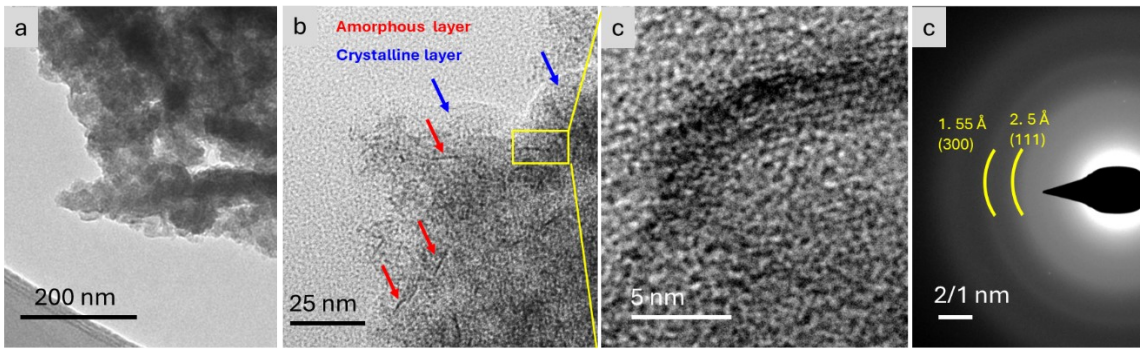


**Fig. S10** (a) TEM, (b) HR-TEM, and (c) SAED pattern of the $NiMoO_4 \cdot xH_2O$ after dipping it in 1 M KOH solution. The atomic plane distance (for the (100) exposed plane) and SAED rings imply the formation of $3Ni(OH)_2 \cdot 2H_2O$.

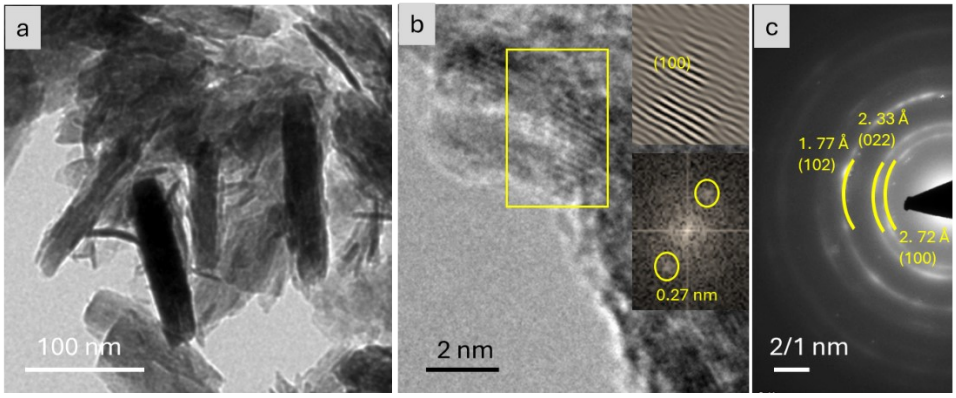


**Fig. S11** (a) TEM, (b) HR-TEM, and (c) SAED pattern of the $CoMoO_4 \cdot xH_2O$ after dipping it in 1 M KOH solution. The atomic plane distance (for (100) exposed plane) and (c) SAED rings imply the formation of β-$Co(OH)_2$.

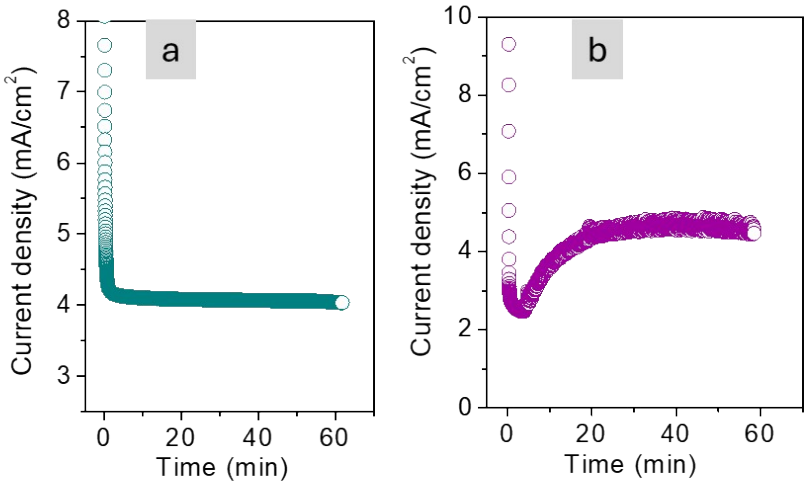


**Fig. S12** Electrochemical activation of the (a) $NiMoO_4 \cdot xH_2O$ (b) $CoMoO_4 \cdot xH_2O$ at 1.6 $V_{RHE}$ in 1 M KOH solution. The activation was performed after the (pre)catalysts had been completely transformed in 1 M KOH, without any potential. After activation, these FTO films were used directly for CV, Tafel, and conductivity analysis.

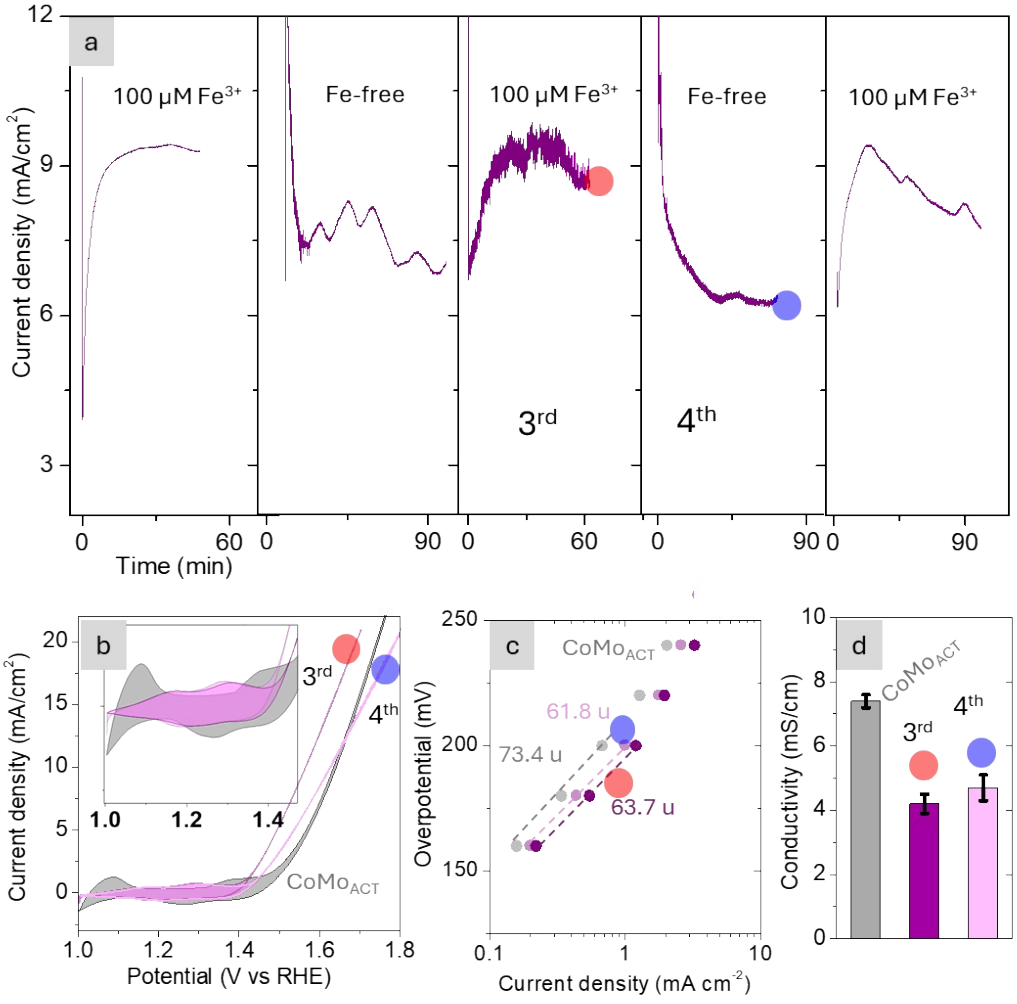


**Fig. S13** (a) Electrochemical cycling of the activated $CoMoO_4 \cdot xH_2O$ ($CoMo_{ACT}$) in the presence and absence of $Fe^{3+}$ in the electrolyte (1 M KOH) solution. The electrochemical activation of $CoMoO_4 \cdot xH_2O$/FTO film is shown in **Figure S12**. In this experiment, same FTO/catalyst film is used for five cycles. After finishing the 3rd (CA in presence of $Fe^{3+}$) and 4th (CA in absence of $Fe^{3+}$) cycles (b) CV, (c) steady state Tafel plot, and (d) film conductivity were measured. For CV and Tafel analysis, the same solution is used as for the 3rd and 4th cycles (Figure a). These performances are compared with activated $CoMoO_4 \cdot xH_2O$ ($CoMo_{ACT}$) in the absence of $Fe^{3+}$ in the solution (all grey coloured profiles). In the Tafel analysis, "u" refers to mV/dec

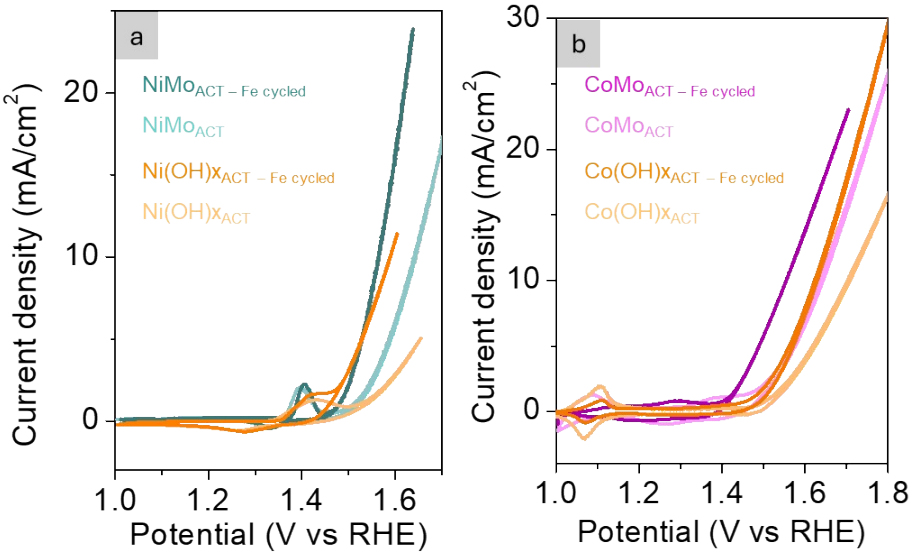


**Fig. S14**. Activity comparison with CV profile for the (a) $NiMo_{ACT}$, $Ni(OH)_2$, and (b) $CoMo_{ACT}$, $Co(OH)_2$ cycled with $Fe^{3+}$ in the electrolyte solution. The figure is incorporated in the supporting information.

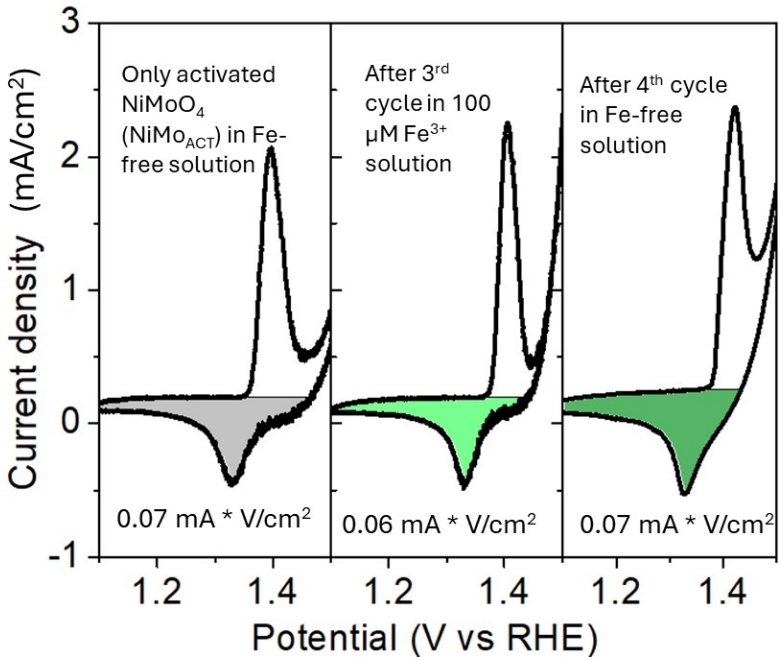


**Fig. S15** Integration and corresponding charge estimation of the $Ni^{3+}/Ni^{2+}$ redox peak obtained from the CV at different conditions. The activation, 3rd and 4th cycles are shown in Figure 3a.

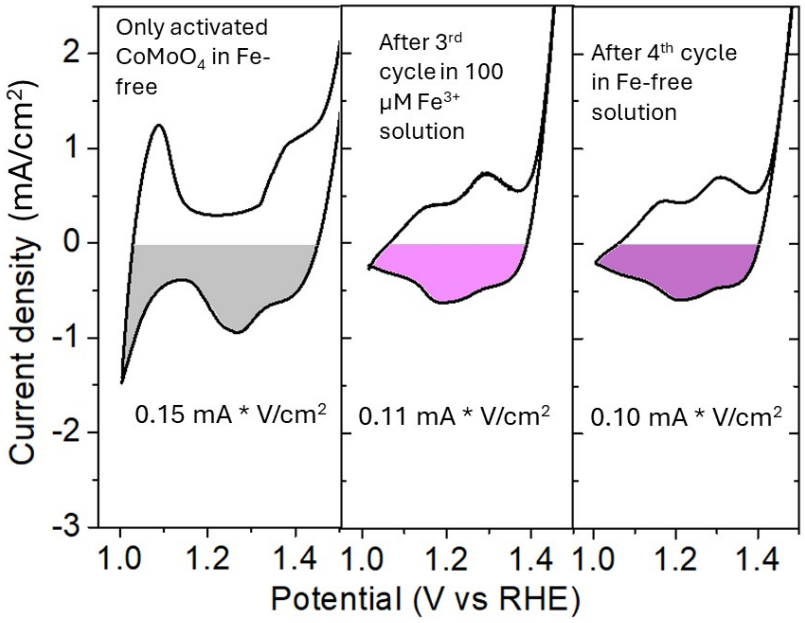


**Fig. S16** Integration and corresponding charge estimation of the $Co^{3/4+}/Co^{2+}$ redox peak obtained from the CV at different conditions. The activation, 3rd and 4th cycles are shown in Figure 13a.

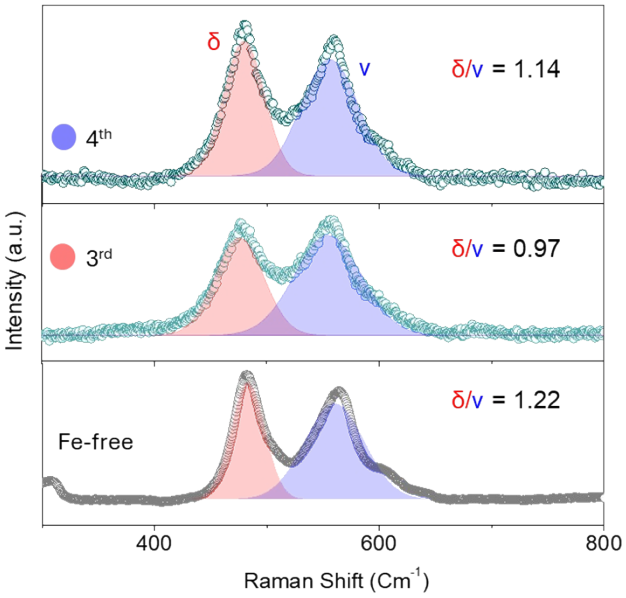


**Fig. S17** The *In-situ* Raman spectroscopy of the activated $NiMoO_4 \cdot xH_2O$ ($NiMo_{ACT}$) with peak fitting at 482cm$^{-}$(δ) and 560cm$^{-1}$(ν). The ratio δ/ν was estimated using the intensity of the spectra, rather than the area of the profile. Before fitting the bands, the baseline was corrected. The middle spectra were taken after the 3$^{rd}$ (in the presence of $Fe^{3+}$) and 4$^{th}$ (Fe-free, top spectra) cycling (as shown in Fig. 3a) using the same electrolyte solution. These experiments were conducted using the same catalyst/FTO film.

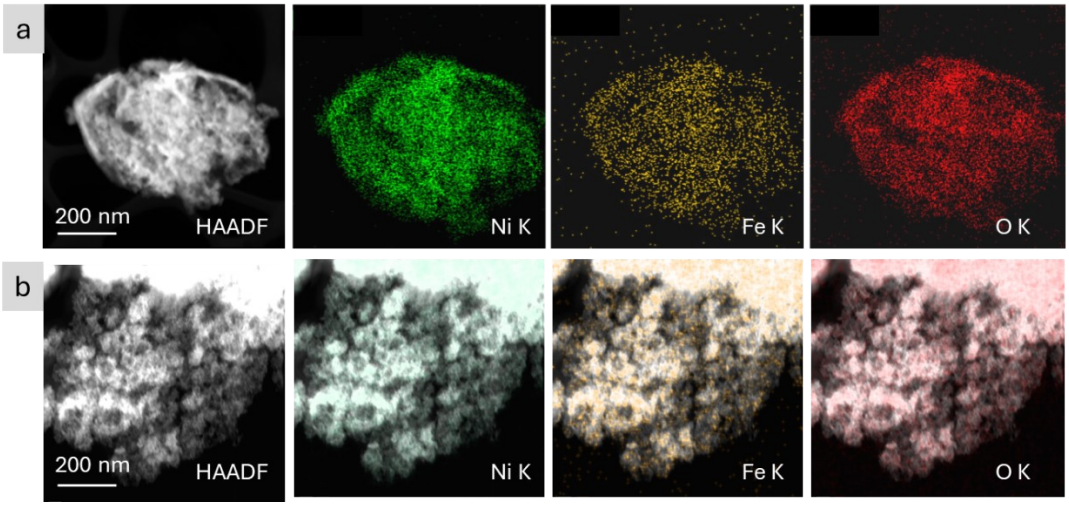


**Fig. S18** TEM HAADF and corresponding elemental mapping for the activated NiMo (a) after cycling in the presence of $Fe^{3+}$ (at 3$^{rd}$ cycle) and (b) the same sample after 4$^{th}$ cycle, where chronoamperometry was carried out in the Fe-free electrolyte (see Figure 3a). The result indicates a homogeneous Fe distribution and no significant phase segregation.

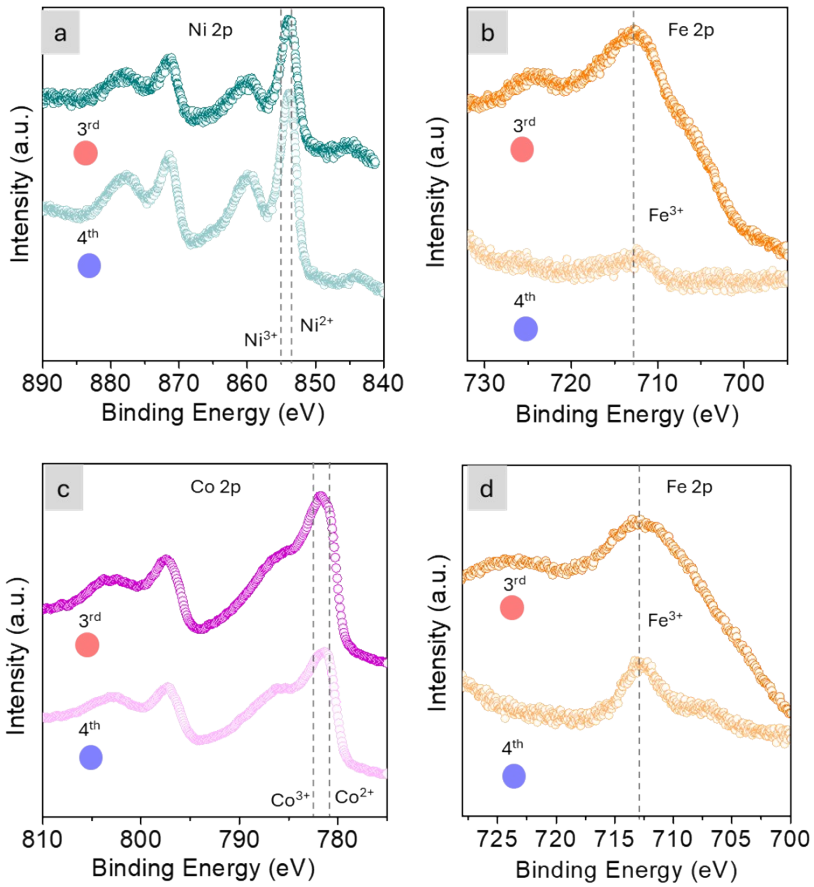


**Fig. S19** High resolution XPS profile of (a,b) $NiMo_{ACT}$ and (c,d) $CoMo_{ACT}$ after $Fe^{3+}$ cycling. (a) Ni 2p and (b) Fe 2p profile of the $NiMo_{ACT}$ catalysts and (c) Co 2p and (d) Fe 2p profile of the $CoMo_{ACT}$ catalyst recorded after the 3rd and 4th cycle (for cycle please see Figure 3).

## Reference


1 I. Mondal, J. N. Hausmann, G. Vijaykumar, S. Mebs, H. Dau, M. Driess and P. W. Menezes, *Adv. Energy Mater.*, 2022, **12**, 2200269.

2 J. N. Hausmann, B. Traynor, R. J. Myers, M. Driess and P. W. Menezes, *ACS Energy Lett.*, 2021, **6**, 3567–3571.

3 L. Trotochaud, S. L. Young, J. K. Ranney and S. W. Boettcher, *J. Am. Chem. Soc.*, 2014, **136**, 6744–6753.

4 M. Nishimoto, I. Muto, Y. Sugawara and N. Hara, *J. Electrochem. Soc.*, 2019, **166**, C3081–C3089.